

Modeling of Cavern Formation in Yield Stress Fluids in Stirred Tanks

Qi Xiao

State Key Laboratory of Multiphase Flow in Power Engineering, Xi'an Jiaotong University, Xi'an, Shaanxi 710049, P.R. China

State Key Laboratory of Multiphase Complex Systems, Institute of Process Engineering, Chinese Academy of Sciences, Beijing 100190, P.R. China

Ning Yang

State Key Laboratory of Multiphase Complex Systems, Institute of Process Engineering, Chinese Academy of Sciences, Beijing 100190, P.R. China

Jiahua Zhu

School of Chemical Engineering, Sichuan University, Chengdu, Sichuan 610065, P.R. China

Liejin Guo

State Key Laboratory of Multiphase Flow in Power Engineering, Xi'an Jiaotong University, Xi'an, Shaanxi 710049, P.R. China

DOI 10.1002/aic.14470

Published online April 25, 2014 in Wiley Online Library (wileyonlinelibrary.com)

Prediction of cavern formation in yield stress fluids in stirred tanks is of great importance for optimization. A new torus model is developed and then validated by experimental data and computational fluid dynamics simulation. Unlike existing mathematical models, the new torus model assumes that the circular center of the torus should not be outside the impeller swept region as the Reynolds number (Re) increases. Hence the cavern boundary is shaped like an apple torus rather than a horn torus. The new model also considers the cavern-vessel interactions. At relatively high Re, the new model predicts cavern shape and size better than other models. It correctly captures the cavern outline at various Re, which verified the assumption about torus center. The new model is then used to identify the influence of rheological parameters on cavern formation, and further extended to the cavern prediction of the dual-impeller system. © 2014 American Institute of Chemical Engineers AICHE J, 60: 3057–3070, 2014

Keywords: computational fluid dynamics, stirred tank, yield stress, cavern

Introduction

Mixing, as an important unit operation in chemical engineering, is frequently needed in chemical and mineral processing, pulp and paper manufacturing, wastewater treatment, and the food industry. To acquire a thorough understanding of the phenomena that occur in mixing tanks and thereby optimize these processes, a large number of experimental, theoretical, and computational fluid dynamics (CFD) studies have been carried out in recent decades (see Joshi et al.¹ and Nere et al.² for reviews). Most of these studies focused on Newtonian fluids, and the mixing of non-Newtonian fluids has received less attention. However, the operating fluids in practical situations often involve proteins, polymers, or very fine particles that exhibit non-Newtonian characteristics and yield stress (e.g.,

slurries in mineral processing, pulp suspensions, and fluids in the human body). Because of their complex rheology, the flow behavior of non-Newtonian fluids deviates markedly from that of Newtonian fluids. Understanding the mixing of non-Newtonian fluids with yield stress is a great challenge.^{3–7}

It has been observed experimentally that the agitation of non-Newtonian fluids with yield stress or highly shear-thinning fluids usually leads to the formation of cavern and stagnant regions.⁸ A cavern is defined as a well-mixed zone around the impeller, whereas the stagnant region outside is poorly mixed, which is undesirable. Identifying the cavern size and shape are important for process design and optimization.

A number of experimental techniques have been used to characterize cavern formation such as hot-film anemometry, planar laser-induced fluorescence, laser Doppler anemometry (LDA), ultrasonic Doppler velocimetry (UDV), particle image velocimetry, positron emission particle tracking (PEPT), and electrical resistance tomography (ERT).⁹ Solomon et al.⁸ used hot-film anemometry to capture the cavern boundaries for fluids with yield stress (carbopol and xanthan gum solutions) or without yield stress (carboxymethyl

Additional Supporting Information may be found in the online version of this article.

Correspondence concerning this article should be addressed to N. Yang at nyang@ipe.ac.cn and J. Zhu at jhzhu@scu.edu.cn.

© 2014 American Institute of Chemical Engineers

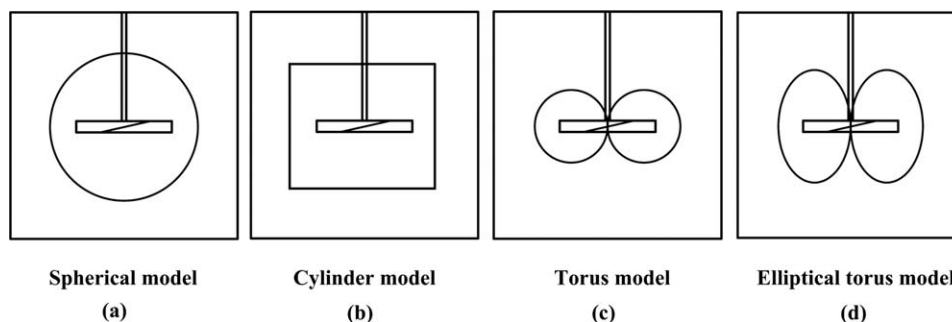


Figure 1. Existing cavern models.

cellulose (CMC) solutions) stirred by a Rushton impeller. They only observed a pseudocavern in CMC solutions because the fluid in the mixing tank was always in motion. In contrast, for the working fluids with yield stress, the boundary between cavern and stagnant region was readily distinguished. They proposed the spherical model to describe caverns. Elson et al.¹⁰ used the X-ray heavy-metal tracer technique to detect cavern formation in working fluids of xanthan gum using four similar Rushton impellers. A right circular cylinder was found to describe the cavern better than a sphere, and larger caverns were obtained for larger impellers at the same power number. Although the above x-ray technique is nonintrusive and suitable for opaque fluids, it is limited by the X-ray opacity of the fluid. The colored or florescent dye injection technique facilitates visualization, and has also been used to study cavern formation in the mixing of carbopol or xanthan gum solutions.^{5,6,11–14} Some researchers used LDA to investigate the fluid dynamics inside caverns. By analyzing the velocity fields inside the mixing tank, the cavern boundary was determined.^{15–17} Both the dye injection and LDA techniques are restricted to transparent fluids but most non-Newtonian fluids are opaque. Other more advanced experimental methods such as UDV, ERT, and PEPT can overcome the opaque limitation and have been used to investigate cavern formation in non-Newtonian mixing on the laboratory scale.^{18–22} However, the accuracy, robustness, ease of application, and applicability of these methods for the industrial scale still require improvements.

CFD simulation has become a powerful approach that can offer detailed insight into a flow. Arratia et al.⁶ simulated the laminar and transitional flow of shear-thinning fluids with yield stress agitated by single- or triple-Rushton impellers in a stirred tank. They found that numerical simulation correctly predicted the main features of the systems such as cavern formation and cavern–cavern segregation for multiple-impeller systems. They also investigated the stretching fields and scaling behavior and found that at different scales, the cavern size followed a similar relationship with Re and cavern–cavern segregation always existed in multiple-impeller systems even at relatively high Re . Adams and Barigou⁵ investigated the formation of caverns inside a stirred tank with a pitched blade turbine (PBT) by both CFD and experimental methods. The CFD simulation accurately predicted cavern size and shape at low Re , but deviations became considerable at higher Re . The torus model performed better for the prediction of cavern (fluids with yield stress) and pseudocavern (fluids without yield stress) at higher Re compared with the spherical and cylindrical

models. Bakker et al.³ simulated cavern formation in agitated tanks and mechanical flotation cells. They assessed different turbulence models and recommended the shear-stress transport (SST) $k\text{-}\omega$ model. They also reported that the flows of non-Newtonian fluids and water behaved very differently even at the same rotational speed and fluid rheology had a noticeable effect on cavern characteristics. For example, the cavern size decreased with increasing yield stress or Bingham viscosity.

Compared with experimental and CFD methods, some cavern models can easily estimate cavern shape and size using just several measurable parameters (such as yield stress, rotational speed, power input, or axial force). By assuming that the shear stress at the cavern boundary equals the yield stress and torque acts tangentially, Solomon et al.⁸ proposed a spherical model (Figure 1a) through torque balance analysis

$$\left(\frac{D_C}{D}\right)^3 = 4 \left(\frac{\rho D^2}{\pi^3 \tau_y}\right) (N_p N^2) \quad (1)$$

where D_C , D , N , N_p , and τ_y are the cavern diameter, impeller diameter, impeller speed, power number, and yield stress, respectively. However, they pointed out that the assumption of spherical cavern shape may not be strictly correct.⁸

Then, Elson et al.^{10,23,24} suggested that it was more reasonable to model the cavern as a right circular cylinder centered on the impeller (Figure 1b) and calculated the cavern diameter from

$$\left(\frac{D_C}{D}\right)^3 = \frac{1}{\pi^2 \left(\frac{H_C}{D_C} + \frac{1}{3}\right)} N_p \left(\frac{\rho N^2 D^2}{\tau_y}\right) \quad (2)$$

where H_C denotes the cavern height. H_C/D_C is a constant depending on the impeller type before the cavern reaches the vessel wall, while afterward the cavern height H_C is proportional to N^p , where p is also a constant related to the impeller type.

Unlike the spherical and cylindrical models, Amanullah et al.¹³ took both the tangential and axial force components into account, which made their model applicable for both radial- and axial-flow impellers. A torus with a zero inner radius was used to model the cavern shape (Figure 1c). The circle radius of the torus was calculated according to

$$\left(\frac{2r_C}{D}\right)^2 = \frac{1}{\pi^2} \sqrt{N_f^2 + \left(\frac{4N_p}{3\pi}\right)^2} \left(\frac{\rho N^2 D^2}{\tau_y}\right) \quad (3)$$

where $N_f = F_a/(\rho N^2 D^4)$ is the dimensionless axial force number and F_a is the axial force.¹³

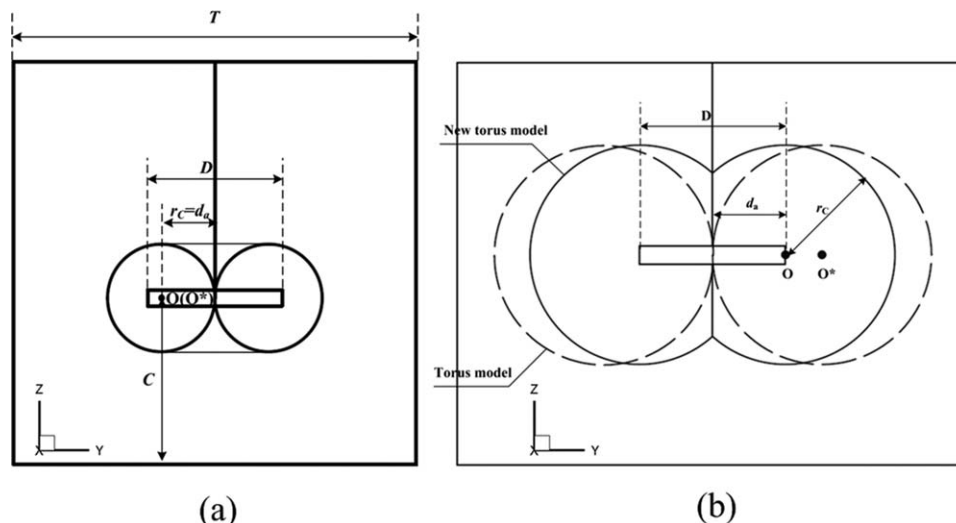


Figure 2. Comparison of torus models: (a) $r_C < D/2$; (b) $r_C > D/2$.

Hui et al.²² adapted the axial force model and developed a truncated right circular cylinder model for side-entering axial-flow impellers by considering the interaction between cavern and vessel wall. Wilkens et al.²⁵ further developed an elliptical torus model (Figure 1d) considering only the tangential effect

$$D_C = \left(\frac{32M}{\pi^2 \alpha \tau_y} \right)^{1/3} \quad (4)$$

$$H_C = \frac{\beta D_C}{2} \quad (5)$$

where $M (= \pi^2 \alpha \tau_y D_C^2 / 32)$ is the torque imparted by the impeller, β is the ratio of the major axis to the minor axis and α is a function of β . α and β depend on the impeller type. The elliptical torus model is limited to radial flow impellers because the axial force is neglected.

The spherical, cylinder, and elliptical torus models only consider the tangential effects and neglect the axial effects, which is not suitable for axial flow impellers. Although experiments have revealed that the cavern shape is more like a torus than a sphere or cylinder,^{5,6,25} the existing torus model is limited to the condition where the cavern has not reached the vessel wall. And, at relatively high Re , the cavern shifts from a horn torus, used in the existing torus model, to an apple torus. This article proposes a new torus model assuming that the circle center of the torus should be located within the impeller swept region. When the circular radius of the torus is larger than the impeller radius, the center of the circle remains at the impeller tip and the predicted cavern turns into an apple torus. Furthermore, the new torus model is extended to situations where the cavern reaches the vessel wall, which is often encountered in experiments and industry, by considering the cavern-wall interactions. The new torus model is validated with experimental data from the literature⁵ and obtained in CFD simulation. We then try to select an appropriate CFD strategy (determination of turbulence model and grid size) to correctly simulate the hydrodynamics inside the mixing tank. The influence of each rheological parameter on the cavern formation is also investigated by both CFD simulation and the new torus model.

Cavern formation in a dual-impeller system is also studied by CFD simulations and the new torus model.

New Torus Model

On one hand, the total force imparted by an impeller can be expressed as

$$F = \rho N^2 D^4 \sqrt{N_f^2 + \left(\frac{4N_p}{3\pi} \right)^2} \quad (6)$$

according to the axial force model of Amanullah et al., and should be balanced by the total force acting on the cavern boundary.^{13,22} On the other hand, the force acting on per unit area at the interface between the stagnant region and cavern is equal to the yield stress τ_y . If the cavern is assumed to be a horn torus as shown in Figure 2, the following equation can be derived

$$F = \tau_y S_p = \tau_y \cdot \pi^2 (2r_C)^2 \quad (7)$$

where S_p denotes the cavern-stagnant interface area, and r_C is the circular radius of the torus. Combining Eqs. 6 and 7 yields Eq. 3 to calculate r_C . Taking the impeller center as the point of origin and z as the rotation axis, the horn torus model developed by Amanullah et al.¹³ for fluids with yield stress can be expressed in Cartesian coordinates (Figure 2)

$$(r_C - \sqrt{x^2 + y^2})^2 + z^2 = r_C^2 \quad (8)$$

$$\tau_y \cdot \pi^2 (2r_C)^2 = \rho N^2 D^4 \sqrt{N_f^2 + \left(\frac{4N_p}{3\pi} \right)^2} \quad (9)$$

In this model, the circle center of the torus (O^* in Figure 2) moves along the impeller as the cavern grows, and is allowed to be far outside the impeller zone. In this case, $r_C = d_a > D/2$ (Figure 2b), where d_a denotes the distance between the circle center and the rotation axis. This keeps the two circles from overlapping and r_C is always equal to d_a .

However, because it is the impeller that motivates the working fluids inside the mixing tank and a high shear rate

usually occurs around the impeller,^{26–28} the center of the circle should be kept within the impeller swept region: that is, $d_a \leq D/2$. When r_C is less than the impeller radius ($r_C < D/2$), $r_C = d_a < D/2$ and the original torus model of Amanullah et al.¹³ still applies. But when $r_C > D/2$, the circle center (O in Figure 2b) should remain at the impeller tip ($d_a = D/2$) rather than being outside the impeller swept region as is assumed in the original torus model. Thus, the

left and right sides of the torus can overlap each other, and the cavern surface turns into an apple torus as shown in Figure 2b. In this case, the cavern boundary changes to be

$$\left(\min \left(r_C, \frac{D}{2} \right) - \sqrt{x^2 + y^2} \right)^2 + z^2 = r_C^2 \quad (10)$$

where the first term on the left side, $\min(r_C, D/2)$, restricts the circle center O within the impeller swept region.

Table 1. The New Torus Model

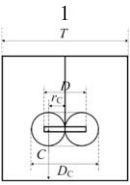
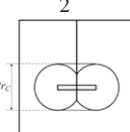
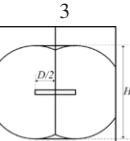
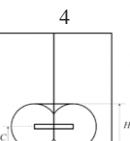
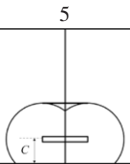
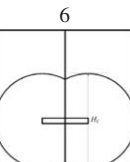
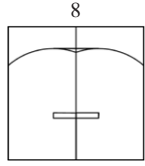
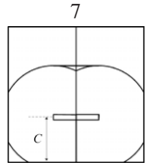
The new torus model	$\left(\min \left(r_C, \frac{D}{2} \right) - \sqrt{x^2 + y^2} \right)^2 + z^2 = r_C^2$	(11)
	$\tau_y(S_p + KS_v) = \rho N^2 D^4 \sqrt{N_f^2 + \left(\frac{4N_p}{3\pi} \right)^2}$	(12)
Case	Cavern surface area (S_p and S_v)	
	For $r_C < D/2$: $S_p = \pi^2 (2r_C)^2$ $S_v = 0$	(13)
	For $r_C \in \left[D/2, \min \left(C, \frac{T-D}{2} \right) \right]$: $S_p = \left(\pi - \arccos \left(\frac{D}{2r_C} \right) \right) \pi (2r_C)^2$ $S_v = 0$	(14)
	For $r_C \in \left[\frac{T-D}{2}, C \right]$ and $T-D \leq 2C$: $S_p = \left(\arcsin \frac{D}{2r_C} + \arcsin \frac{T-D}{2r_C} \right) \pi (2r_C)^2$ $S_v = \pi T \sqrt{(2r_C)^2 - (T-D)^2}$	(15)
	For $r_C \in \left[C, \sqrt{\frac{D^2}{4} + C^2} \right]$ and $T-D \geq \sqrt{D^2 + 4C^2}$: $S_p = \left(\pi - \arccos \frac{C}{r_C} - \arccos \frac{D}{2r_C} \right) \pi (2r_C)^2$ $S_v = \pi D \sqrt{(2r_C)^2 - 4C^2}$	(16)
	For $r_C \in \left[\sqrt{\frac{D^2}{4} + C^2}, \frac{T-D}{2} \right]$: $S_p = \left(\frac{3\pi}{2} - \arccos \frac{C}{r_C} - \arccos \frac{D}{2r_C} \right) \frac{\pi}{2} (2r_C)^2$ $S_v = \frac{\pi}{4} \left(D + \sqrt{(2r_C)^2 - 4C^2} \right)^2$	(17)
	For $r_C \in \left[\max \left(C, \frac{T-D}{2} \right), \sqrt{C^2 + \frac{D^2}{4}} \right]$: $S_p = \left(\pi - \arccos \frac{C}{r_C} - \arccos \frac{D}{2r_C} - \arccos \frac{T-D}{2r_C} \right) \pi (2r_C)^2$ $S_v = \pi D \sqrt{(2r_C)^2 - 4C^2} + \pi T \sqrt{(2r_C)^2 - (T-D)^2}$	(18)

TABLE 1. Continued



$$\text{For } r_C \in \left[\max \left(\sqrt{\frac{D^2}{4} + C^2}, \frac{T-D}{2} \right), \sqrt{C^2 + \frac{(T-D)^2}{4}} \right] :$$

$$S_p = \left(\frac{3\pi}{2} - \arccos \frac{C}{r_C} - \arccos \frac{D}{2r_C} - 2\arccos \frac{T-D}{2r_C} \right) \frac{\pi}{2} (2r_C)^2 \quad (19)$$

$$S_v = \frac{\pi}{4} \left(D + \sqrt{(2r_C)^2 - 4C^2} \right)^2 + \pi T \sqrt{(2r_C)^2 - (T-D)^2}$$

$$\text{For } r_C > \sqrt{\frac{(T-D)^2}{4} + C^2} :$$

$$S_p = \left(\arcsin \frac{D}{2r_C} + \arcsin \frac{T-D}{2r_C} \right) \frac{\pi}{2} (2r_C)^2 \quad (20)$$

$$S_v = \frac{\pi T^2}{4} + \pi T \left(C + \sqrt{(r_C)^2 - \left(\frac{T-D}{2} \right)^2} \right)$$

Another issue in the new torus is the cavern-wall interaction. Further increasing the rotational speed, the cavern may touch the vessel wall and the torus becomes truncated. Table 1 illustrates the different cases of cavern-stagnant and cavern-wall interactions. The total force acting on the cavern surface changes to²²

$$F = \tau_y S_p + \tau_v S_v \quad (21)$$

where S_v is the surface area of the cavern-vessel contact and τ_v is the wall friction force acting on per unit cavern-vessel area. It can be reasonably assumed that $\tau_v = K\tau_y$, where K is greater than 1 because the yield stress must be overcome to drive the working liquid. Equation 21 can thus be reformulated as

$$F = \tau_y (S_p + KS_v) \quad (22)$$

K is a constant as a first approximation. Combining Eqs. 6 and 22 leads to

$$\tau_y (S_p + KS_v) = \rho N^2 D^4 \sqrt{N_f^2 + \left(\frac{4N_p}{3\pi} \right)^2} \quad (23)$$

Equations 10 and 23 give a new torus model, and when the circular radius is small [$r_C < \min(D/2, C, T/4)$], the new torus model is reduced to the torus model. To obtain the cavern size r_C for different cases in Table 1, S_p and S_v should be determined analytically. Taking the Case 6 as an example (Figure 3), the cavern-stagnant surface can be analytically formulated as

$$S_p = \frac{1}{2} (2\pi - 2\alpha_1 - 2\alpha_2 - 2\alpha_3) \pi (2r_C)^2 = (\pi - \alpha_1 - \alpha_2 - \alpha_3) \pi (2r_C)^2 \quad (24)$$

$$\alpha_1 = \arccos \left(\frac{D}{2r_C} \right) \quad (25)$$

$$\alpha_2 = \arccos \left(\frac{T-D}{2r_C} \right) \quad (26)$$

$$\alpha_3 = \arccos \frac{C}{r_C} \quad (27)$$

The cavern-wall surface area is composed of the cavern-vessel interface (S_1) and cavern-bottom interface (S_2)

$$S_v = S_1 + S_2 \quad (28)$$

$$S_1 = \pi D \sqrt{(2r_C)^2 - 4C^2} \quad (29)$$

$$S_2 = \pi T \sqrt{(2r_C)^2 - (T-D)^2} \quad (30)$$

S_p and S_v are functions of torus radius r_C , and we are thus in a position to determine the torus radius r_C by simple iterations using Eq. 23.

CFD Simulation

CFD simulation is used to obtain more detailed information about the cavern formation, the power and axial force numbers and then validate the new torus model. The configuration of the simulated single-impeller mixing tank is the same as that in the experiment published by Adams and Barigou.⁵ For the dual-impeller system, the height of the mixing tank is augmented to 0.2 m to avoid the influence of the top surface (Figure 4)

The working fluid is a 0.1 wt % aqueous solution of carbopol and its rheology can be described by the Herschel–Bulkley equation

$$\tau = \tau_y + k\dot{\gamma}^n \quad (31)$$

$$\mu = \tau\dot{\gamma} = \tau_y\dot{\gamma} + k\dot{\gamma}^{n+1} \quad (32)$$

where τ , k , and n represent the shear stress, fluid consistency coefficient, and flow behavior index, respectively. To avoid the denominator having a value of zero at $\dot{\gamma} = 0$, a piecewise equation is adopted

$$\begin{cases} \mu = \mu_y, & \text{for } 0 \leq \dot{\gamma} \leq \tau_y/\mu_y \\ \mu = \frac{\tau_y + k[\dot{\gamma}^n - (\tau_y/\mu_y)^n]}{\dot{\gamma}}, & \text{for } \dot{\gamma} > \tau_y/\mu_y \end{cases} \quad (33)$$

where μ_y is a large number (20,000 kg/m s) to ensure that the slurry behaves as a solid when not being yielded.

The Metzner–Otto correlation is used to calculate the effective viscosity^{29,30}

$$\dot{\gamma}_e = k_s N \quad (34)$$

where the constant $k_s = 11$ for the PBT impeller according to Adams and Barigou.⁵ The effective viscosity and Re can then be calculated from

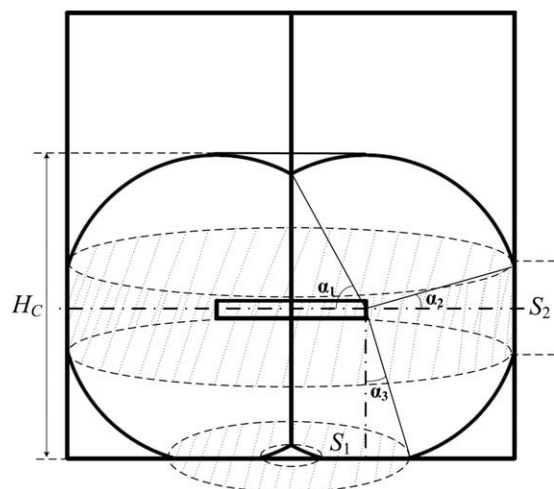


Figure 3. Cavern surface area for Case 6 in Table 1.

$$\mu_e = \frac{\tau_y}{k_s N} + k(k_s N)^{n-1} \quad (35)$$

$$Re = \frac{\rho k_s N^2 D^2}{\tau_y + k(k_s N)^n} \quad (36)$$

Other dimensionless numbers used to evaluate the performance of a mixing tank such as the power number (N_P) and flow number (N_Q), which are related to power consumption and pumping capacity, respectively, are calculated as

$$N_P = \frac{P}{\rho N^3 D^5} \quad (37)$$

$$N_Q = \frac{Q}{ND^3} \quad (38)$$

where P is the power input and Q the axial volume flow rate defined by Nienow³¹ for axial impellers.

The commercial CFD package Fluent 6.3.26 was used for the simulations. In this work, the flow interaction between baffles and impellers is not critical because the distance between them was large, so the multiple reference frames method was adopted to model the impellers. The rotational and inertial frames were used for the domain around the impeller and the outside region, respectively. Both tetrahedral and hexahedral meshes were used to discretize the com-

Table 2. Grid Practical Independence Test

Cases	Mesh Number	Power Number	Flow Number
Grid 1	386,673	2.130	0.415
Grid 2	543,778	1.926	0.501
Grid 3	764,265	2.082	0.456
Grid 4	1,155,863	2.038	0.484
Grid 5	1,305,508	2.030	0.492
Grid 6	1,530,418	2.030	0.490

putational volume and the third-order MUSCL scheme was used to minimize numerical diffusion. The critical residuals for convergence are set to be 10^{-4} and the variation of the impeller moment is also taken as a criterion for convergence.

Grid practical independence

The grid practical independence test was carried out at $Re = 163.2$ ($N = 368$ rpm) with the standard $k-\epsilon$ model. Table 2 shows the power and flow numbers predicted by simulations with six different grids. Figure 5 illustrates the cavern boundary and power and flow numbers. As mentioned by Bakker et al.³, it is reasonable to define the cavern boundary as an isosurface with a strain rate less than 0.2 s^{-1} ; in this study, a critical value of 0.1 was used. Grid practical independence was achieved for mesh numbers of more than 1,155,863: the differences in both cavern shape and size were negligible and the variation of power and flow numbers predicted by CFD was less than 3%. As a compromise between computational cost and accuracy, Grid 4 was used in the following simulation.

Turbulence model

At low rotational speed, the flow inside the stirred tank can be modeled as laminar flow. When the cavern reaches the vessel wall, the impeller speed is higher and the flow around the impeller may be turbulent yet laminar around the cavern boundary. Thus, a turbulence model should be carefully chosen to cover the whole region. Six turbulence models, the laminar, Spalart–Allmaras, standard $k-\epsilon$, renormalization group (RNG) $k-\epsilon$, standard $k-\omega$, and SST $k-\omega$ models, were investigated in this study. The caverns predicted by different models at various Re are presented in Figure 6. At low Re , the $k-\epsilon$ models (including the standard and RNG $k-\epsilon$

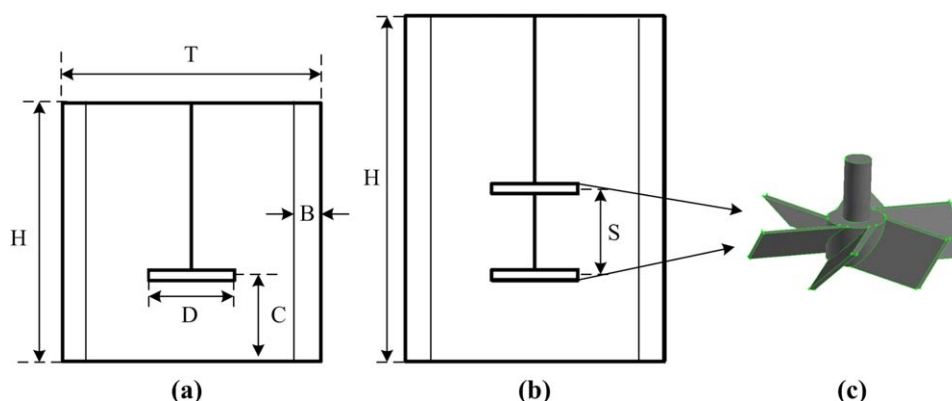


Figure 4. Configurations for single- and dual-impeller system simulations: (a) single-impeller system ($H = T = 0.148 \text{ m}$, $B = 0.1T$, $D = C = T/3$); (b) dual-impeller system ($H = 4/3T$); (c) PBT.

[Color figure can be viewed in the online issue, which is available at wileyonlinelibrary.com.]

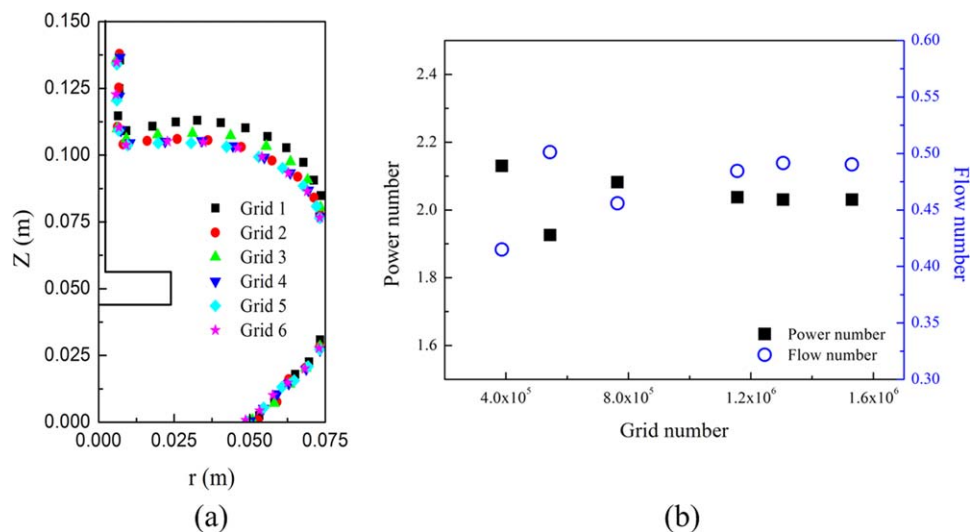


Figure 5. (a) Cavern boundary prediction and (b) power number and flow number for different mesh numbers.

[Color figure can be viewed in the online issue, which is available at wileyonlinelibrary.com.]

models) greatly overpredict the cavern size, while they perform better at relatively high Re . All of the other models can correctly predict the cavern shape and size at various rotational speeds and show little difference. In general, all these

models slightly overpredict the cavern size at low Re , and perform better at high Re .

However, the differences in power and flow numbers predicted by different turbulence models are considerable

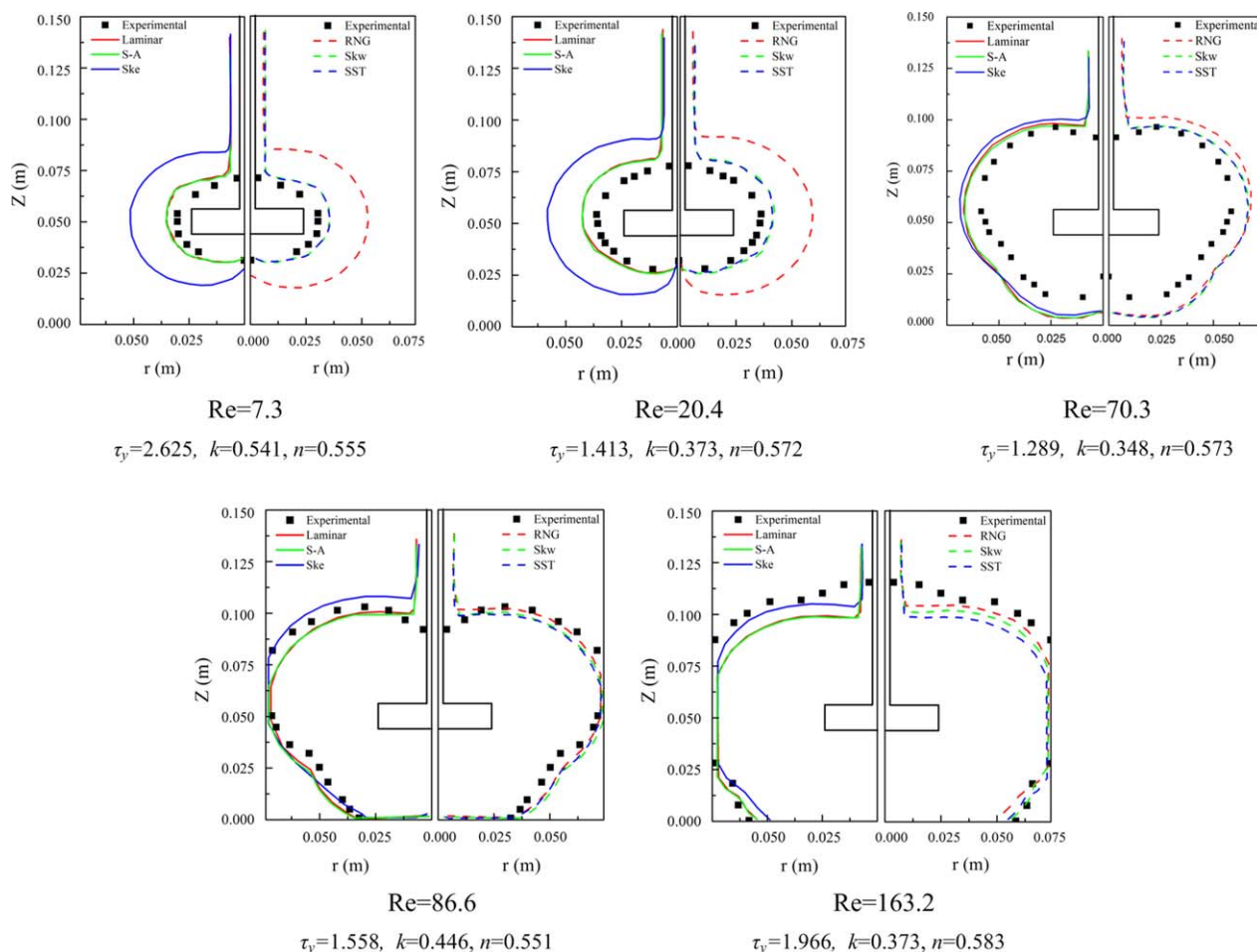


Figure 6. Cavern predicted by different turbulence models.

Here, S-A: Spalart-Allmaras model; Ske: standard $k-\epsilon$ model; RNG: RNG $k-\epsilon$ model; Skw: standard $k-\omega$ model; SST: SST $k-\omega$ model. [Color figure can be viewed in the online issue, which is available at wileyonlinelibrary.com.]

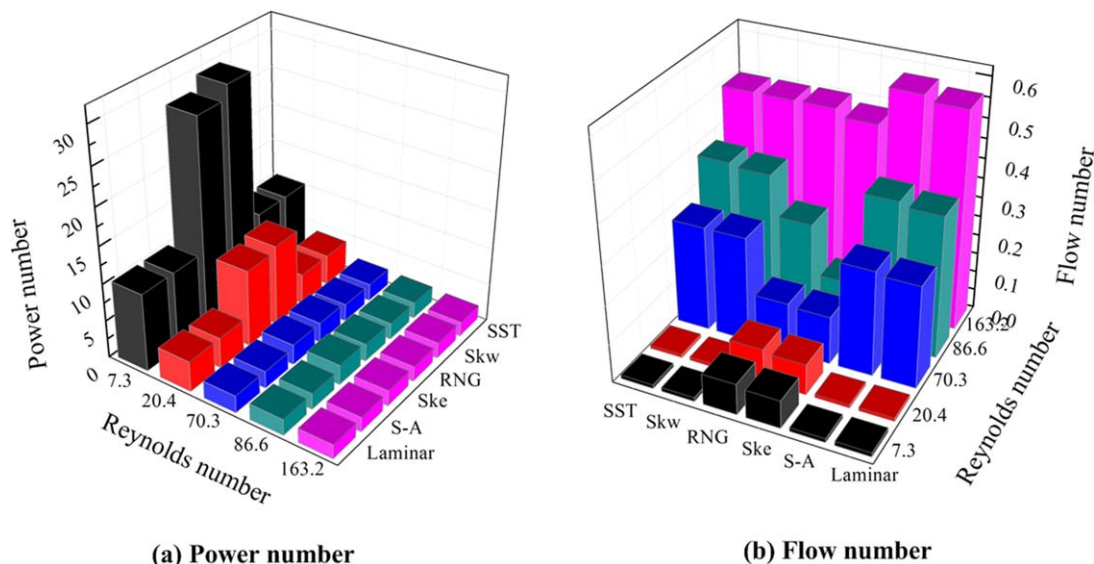


Figure 7. Power and flow numbers predicted by different turbulence models.

[Color figure can be viewed in the online issue, which is available at wileyonlinelibrary.com.]

Table 3. Power and Axial Force Numbers Obtained by CFD Simulation with SST $k-\omega$ Model

Reynolds Number	$Re = 7.3$	$Re = 20.4$	$Re = 70.3$	$Re = 86.6$	$Re = 163.2$
Power number	10.439	4.090	2.287	2.127	1.902
Axial force number	2.943	0.992	0.403	0.402	0.491

(Figure 7). The $k-\epsilon$ models have much higher power numbers than those of other models at low Re . The reason for this may be that the fully turbulent assumption in $k-\epsilon$ models is not suitable for low Reynolds number flow. The standard

and SST $k-\omega$ models have similar forms, however, the SST $k-\omega$ model adopts the $k-\omega$ model near the wall region and the $k-\epsilon$ model in the far field, which makes it more reliable for complex flows.³² The $k-\omega$ models offer similar results to the laminar model at low Re because a low- Re correction was used. As Re increases, turbulence appears and the results obtained by $k-\omega$ models deviate from those of the laminar model and are similar to those of the $k-\epsilon$ models.

Overall, it can be concluded that the laminar and Spalart–Allmaras models perform well at low Re but lose accuracy at high Re ; the $k-\epsilon$ models overpredict the cavern size at low Re ; and the standard and SST $k-\omega$ models may not perform best at every Re but have reasonable predictions at relatively wide range of Re and hence are recommended, which is in accordance with Bakker et al.³ In this article, the SST $k-\omega$ model was used in the following simulation. The power and axial force numbers required in the cavern model were extracted from the CFD simulation, as shown in Table 3.

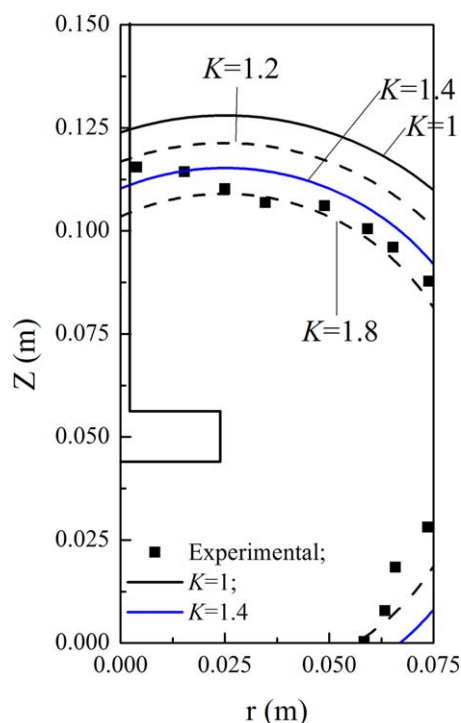


Figure 8. Effect of K on cavern prediction.

[Color figure can be viewed in the online issue, which is available at wileyonlinelibrary.com.]

Validation of the New Torus Model

In this section, the new torus model was compared with other cavern models, and validated using the experimental data obtained at various Re ⁵ as well as CFD simulations. The value of K in Eq. 22 should first be determined by comparison with experimental data, as shown in Figure 8. If $K = 1$ following Hui et al.,²² the wall friction force is equal to the yield stress, and the new torus model greatly overpredicts the cavern size. This suggests that the wall friction force should be larger than the yield stress ($K > 1$). When $K = 1.2$ – 1.8 , the new torus model gives a reasonable prediction, and may vary in different regions. For simplicity, $K = 1.4$ was used in the following study.

CFD simulation offers an insight into the flow field and was used to validate the cavern model. Figure 9 shows the streamlines starting from the impeller and the velocity field calculated by CFD. At $Re = 7.3$, the vortex structure is insignificant and only the upper loop was observed. The torus model and new torus model gave the same prediction and correctly captured the profiles of the streamlines. As Re increases ($Re = 20.4$), the upper and lower vortices develop. The upper loop starts to be interfered with the symmetry axis (the rotational axis), which makes the cavern resemble an apple torus rather than a horn torus, and a difference between the torus model and CFD simulation in cavern prediction emerges. The torus model can roughly capture the cavern size. Further increasing the Re ($Re = 70.3$), the upper and lower vortices become larger and both are truncated by the symmetric axis, which makes the cavern shape greatly deviate from the horn torus. The apple torus predicted by the new torus model successfully captures the streamline profiles of both the upper and lower loops. At $Re = 163.2$, the upper vortex is restricted by the vessel wall while the lower touches the bottom. The original torus model, which does not consider cavern-wall interactions, further deviates from the CFD prediction. Meanwhile, the new torus model takes the cavern-wall interaction into consideration and correctly predicts the profiles of both the upper and lower vortices. It can thus be concluded that at low Re , the vortex structure is insignificant and the torus model can predict the cavern boundary with acceptable tolerance. With increasing Re , the upper and lower vortices grow and become truncated by the symmetric axis. The cavern resembles an apple torus and only the new torus model can capture the profile of streamlines; the original torus model fails. Upon further increasing Re , the upper and lower vortices touch the vessel wall, so cavern-wall interactions should be considered.

Figure 10 compares the cavern boundary predicted by the new torus model with those determined by other cavern models. At low Re ($Re = 7.3$ and 20.4), all mathematical models correctly predict the cavern formation and the cylindrical model shows closest agreement with experimental data. As Re increases, the cylindrical model underpredicts the cavern size because it neglects the axial component, which was also reported by Adams and Barigou.⁵ Other models such as the spherical and original torus models are unsuitable at relatively high Re where the cavern boundary exhibits an apple torus shape ($Re > 20.4$ in Figure 10), especially when the cavern boundary reaches the vessel. Only the new torus model maintains its accuracy in cavern boundary prediction, which is a marked advantage over other cavern models.

As shown above, CFD could correctly predict the cavern boundary and offer more accurate and detailed cavern information at various Re than cavern models. Thus, in the absence of experimental data, CFD could be used to evaluate cavern models. Figure 11 shows the cavern height H_C (defined in Figure 3) predicted by cavern models and CFD simulations at various Re for two fluids with different rheology. The new torus model matches the CFD prediction well for both fluids and provides a much better prediction than the original torus model proposed by Amanullah et al.,¹³ which substantially underestimates cavern height. When the cavern touches the vessel wall (at $Re \sim 75$ in Figure 11a and $Re \sim 85$ in Figure 11b), the increase in cavern height with Re slows, which was captured by CFD and the modified torus model, but not by the original torus model. This also indicates that cavern-wall interactions

should be considered and the wall friction force should be larger than the yield stress.

We then investigated the influence of each rheological parameters on cavern formation with CFD and cavern models at constant rotational speed ($N = 242$ rpm). Because τ_y is the threshold that should be exceeded to make the fluid flow and is directly correlated to the cavern size calculation (Eq. 23), increasing the yield stress markedly decreases cavern size (Figure 12a). Conversely, the CFD results show that the cavern size increases with both n and k (Figures 12b, c). Both the torus and new torus model captured these tendencies, although the new torus model showed better agreements with CFD predictions than the original.

Cavern Formation in a Dual-Impeller System

Multiple-impeller systems are usually encountered in industry. The hydrodynamics and cavern formation in such systems are much more complex than those with a single impeller. At low Re , the interaction between impellers is weak (Figure 13). As the Re increases, the interaction between impellers becomes considerable, which makes the caverns formed by each overlap. At relatively high Re , there are two ways to model cavern formation. In the first approach, the dual-impeller system can be simplified as a single impeller with its center located at the midpoint between the impellers. The power consumption and axial force required in the cavern model are assumed to be the summation of each impeller. Taking the center of the lower impeller as the origin point, this method can be formulated using the torus model as

$$\left(r_C - \sqrt{x^2 + y^2}\right)^2 + \left(z - \frac{S}{2}\right)^2 = r_C^2 \quad (39)$$

$$\left(\frac{2r_C}{D}\right)^2 = \frac{1}{\pi^2} \sqrt{N_{f,T}^2 + \left(\frac{4N_{p,T}}{3\pi}\right)^2} \left(\frac{\rho N^2 D^2}{\tau_y}\right) \quad (40)$$

$$N_{f,T} = \frac{F_{a,T}}{\rho N^2 D^4} = \frac{F_{a,upper} + F_{a,lower}}{\rho N^2 D^4} \quad (41)$$

$$N_{p,T} = N_{p,upper} + N_{p,lower} \quad (42)$$

and using the new torus model as

$$\left(\min\left(r_C, \frac{D}{2}\right) - \sqrt{x^2 + y^2}\right)^2 + \left(z - \frac{S}{2}\right)^2 = r_C^2 \quad (43)$$

$$\tau_y (S_p + K S_v) = \rho N^2 D^4 \sqrt{N_{f,T}^2 + \left(\frac{4N_{p,T}}{3\pi}\right)^2} \quad (44)$$

where S_p and S_v are calculated using Eqs. 13–20, as presented in Table 1. $N_{f,T}$ and $N_{p,T}$ represent the total axial force number and power number, respectively, and can be obtained using Eqs. 41 and 42.

The second approach considers the effect of each impeller separately and can be formulated using the torus model as

$$\left(r_{C,i} - \sqrt{x^2 + y^2}\right)^2 + (z - z_i)^2 = r_{C,i}^2, \quad (i = \text{upper or lower}) \quad (45)$$

$$\left(\frac{2r_{C,i}}{D}\right)^2 = \frac{1}{\pi^2} \sqrt{N_{f,i}^2 + \left(\frac{4N_{p,i}}{3\pi}\right)^2} \left(\frac{\rho N^2 D^2}{\tau_y}\right) \quad (46)$$

and using the new torus model as

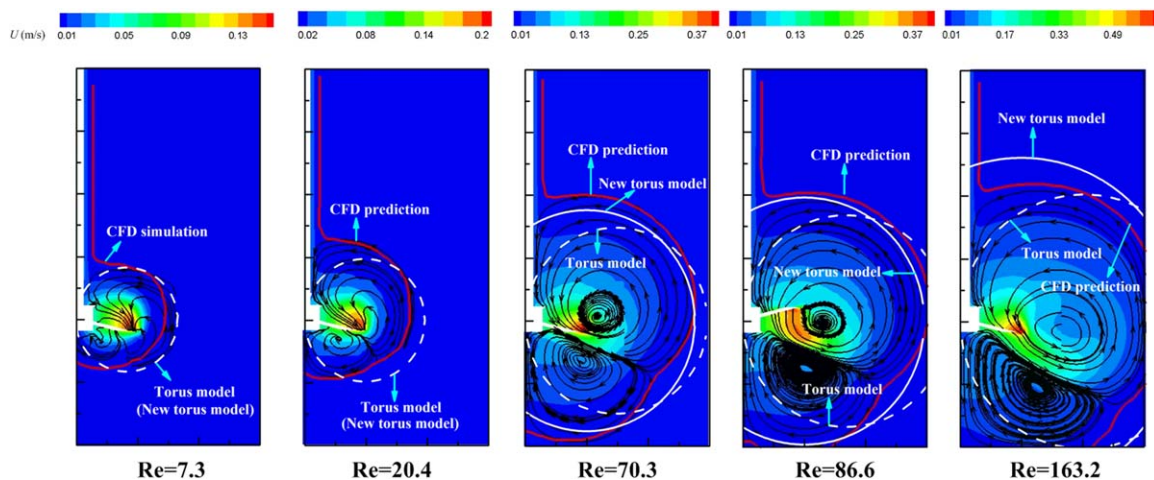
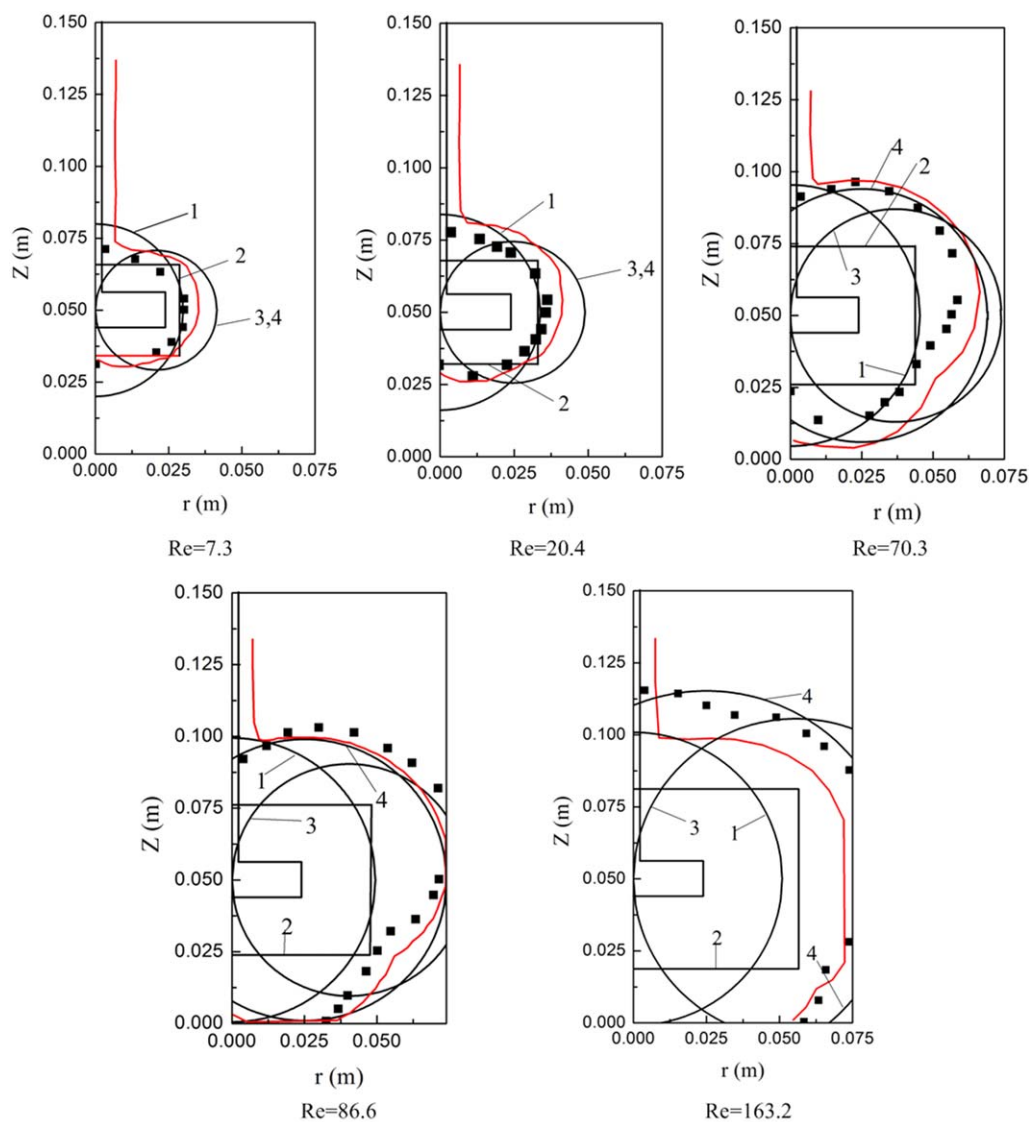


Figure 9. Streamlines and velocity contour at various Re obtained by CFD simulation.

[Color figure can be viewed in the online issue, which is available at wileyonlinelibrary.com.]



■ Experimental; — CFD; 1: Spherical model; 2: Cylindrical model
3: Torus model; 4: New torus model

Figure 10. Comparison of cavern boundary predictions at different Re .

[Color figure can be viewed in the online issue, which is available at wileyonlinelibrary.com.]

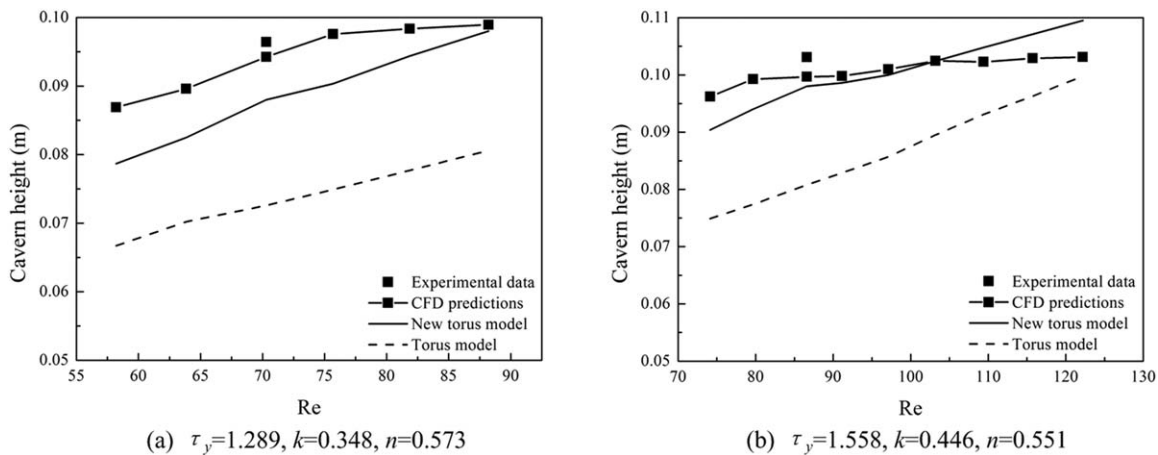


Figure 11. Cavern height predicted by the CFD simulation and different cavern models for fluids with different rheology.

$$\left(\min \left(r_{C,i}, \frac{D}{2} \right) - \sqrt{x^2 + y^2} \right)^2 + (z - z_i)^2 = r_{C,i}^2, \quad (47)$$

(i =upper or lower)

$$\tau_y (S_{p,i} + K S_{v,i}) = \rho N^2 D^4 \sqrt{N_{f,i}^2 + \left(\frac{4N_{p,i}}{3\pi} \right)^2} \quad (48)$$

where S_p and S_v are calculated from equations in Table 1. $z_{\text{lower}} = 0$ and $z_{\text{upper}} = S$ if we take the center of the lower

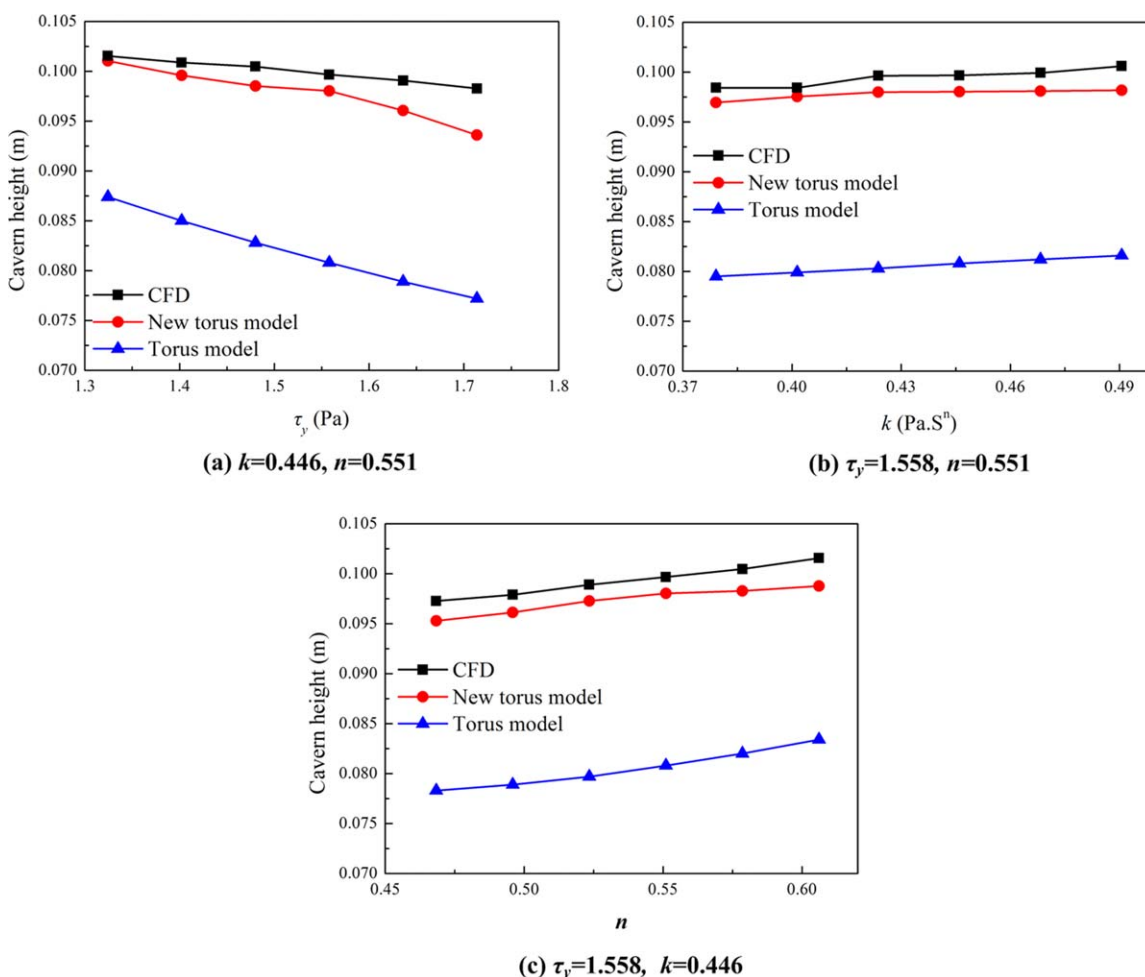


Figure 12. Influence of different rheological parameters on cavern formation at constant rotational speed ($N = 242$ rpm).

[Color figure can be viewed in the online issue, which is available at wileyonlinelibrary.com.]

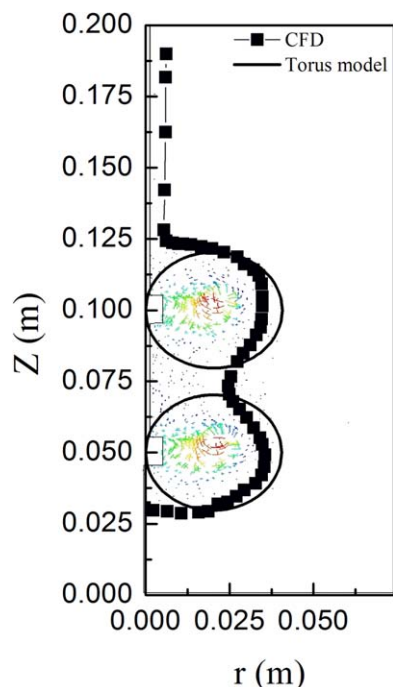


Figure 13. Prediction of low- Re flow for a dual-impeller system ($Re = 7.3$ and $S = D$).

[Color figure can be viewed in the online issue, which is available at wileyonlinelibrary.com.]

impeller as the origin. The first method is suitable in case where the interaction between impellers is strong, whereas the latter is suitable for the case where the interaction between impellers is weaker.

To validate the two methods using both the torus and new torus models, CFD simulations with different impeller spacing (S) were carried out at $Re = 86.6$. As shown in Figures 14 and 15, with increasing impeller spacing, more fluid in the upper zone is stirred by the impellers and the total cavern size increases. The CFD predictions show that the cavern for the dual-impeller system is still shaped more like an apple torus than a horn torus at relatively high Re and touches the vessel wall. The two methods with the original torus model cannot correctly capture the cavern boundary

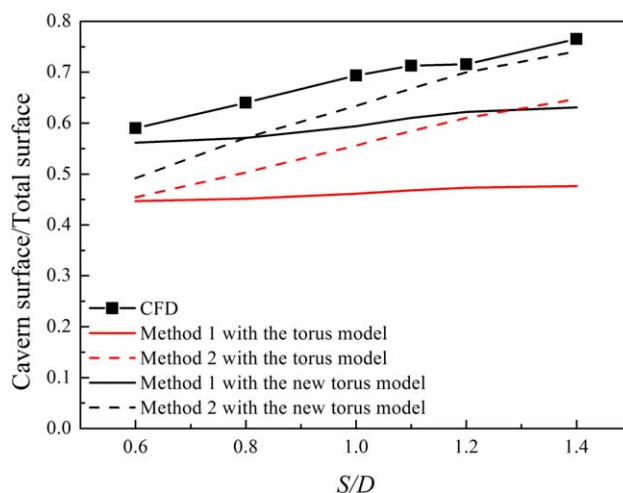


Figure 15. Ratio of cavern area to total area predicted by CFD and the two torus models ($Re = 86.6$).

[Color figure can be viewed in the online issue, which is available at wileyonlinelibrary.com.]

because of the assumption of a horn torus at all Re and because cavern-wall interactions were not considered. In contrast, for the new torus model, both Method 1 and 2 correctly predicted the cavern boundary with acceptable tolerance. At small impeller spacing ($S = 0.6D$), the first method (Eqs. 43 and 44) accurately predicted the cavern size and shape for a dual-impeller system because the interactions between impellers are marked and the performance of the impellers is greatly affected by each other. As the impeller spacing increases, the first method gradually loses its accuracy, whereas the second method (Eqs. 47 and 48) becomes more accurate when the interaction between impellers is weak ($S = 1.4D$).

Both the total power and flow numbers increase with impeller spacing S , as shown in Figure 16. The power number for each impeller is almost the same while the axial flow number of the upper impeller is much larger than that of the lower one, as the axial flow rate of the upper impeller is much larger than that of the lower impeller, as shown in Figure 14. As S increases, the interactions between the impellers

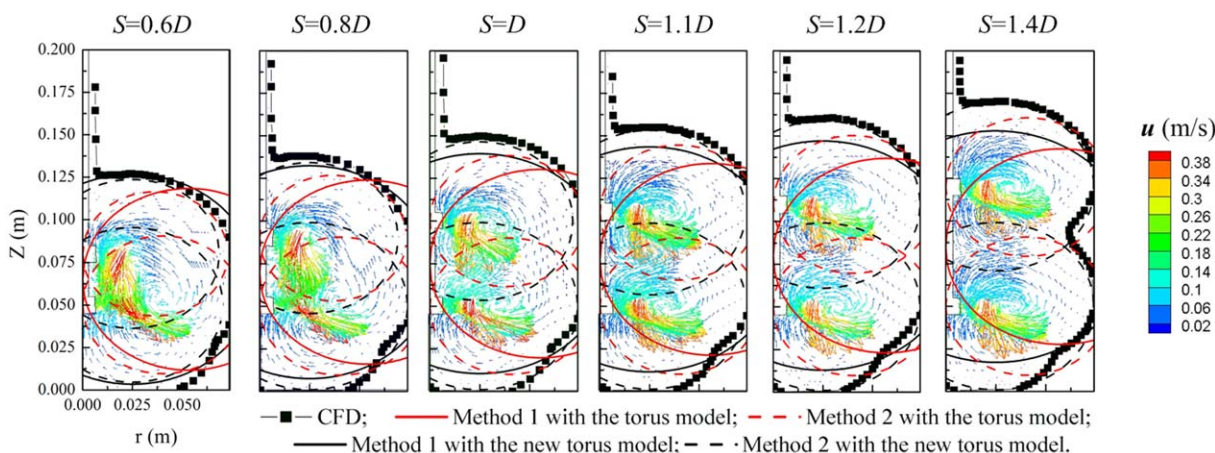


Figure 14. Caverns predicted by CFD and cavern models for a dual-impeller system ($Re = 86.6$).

[Color figure can be viewed in the online issue, which is available at wileyonlinelibrary.com.]

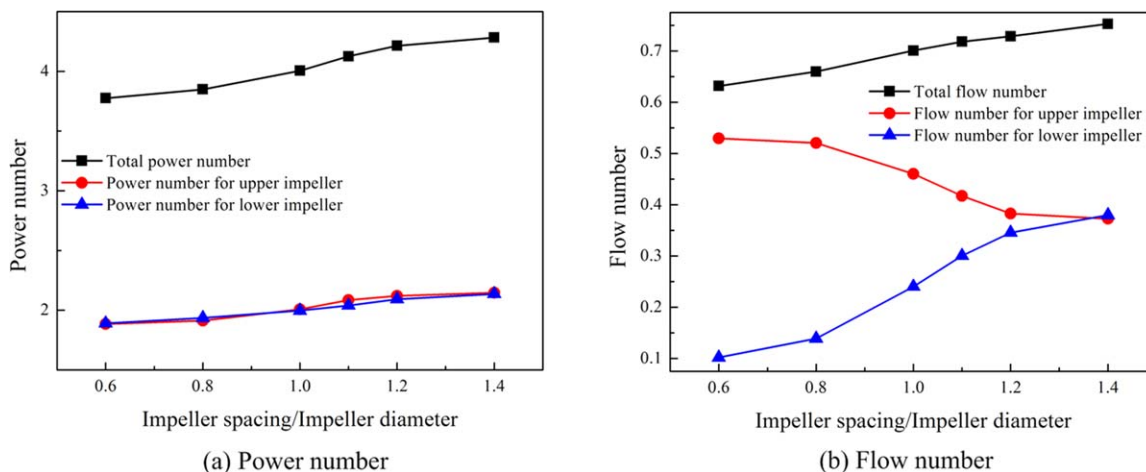


Figure 16. Influence of impeller spacing on the power and flow numbers for a dual-impeller system ($Re = 86.6$).

[Color figure can be viewed in the online issue, which is available at wileyonlinelibrary.com.]

become less important and the flow number for each impeller approaches that of the other.

Conclusions

A new torus model is proposed for the mixing of fluids with yield stress by PBT impeller in baffled stirred tanks and validated by CFD simulation and experiment data from the literature. The new torus model assumes that the circular center should not exceed the impeller swept region ($d_a \leq D/2$), which implies that the cavern boundary is more like an apple torus rather than a horn torus when the cavern grows up. This model also considers the interaction between the cavern and the vessel wall. By comparison with CFD predictions, we confirmed that the new torus model is able to correctly capture the profiles of streamlines at various Re . Compared with the experimental data, all cavern models have acceptable predictions at low Re , while only the new torus model can correctly predict the torus size and shape at higher Re . Both CFD and the new torus model indicate that the growth rate of cavern height with Re slows down when the cavern reaches the vessel. The influence of each rheological parameter can also be analyzed by the new torus model. Compared with the original torus model, the new torus model shows better agreement with CFD simulation. Two methods were proposed to predict cavern formation in a dual-impeller mixing tank: (1) using a single impeller to represent the effects of two impellers with the same total power consumption and axial force; (2) considering the effects of each impeller separately. The CFD results show that the cavern for a dual-impeller system at $Re = 86.6$ is shaped more like an apple torus rather than a horn torus model and touches the vessel wall. The original torus model cannot correctly describe cavern formation in this situation. In contrast, both the methods with the new torus model show acceptable agreements with CFD predictions. It was found that the first method is more suitable for situations where the interaction between impellers is important while the second performs better when the interaction weakens as impeller spacing increases.

Acknowledgment

The author thanks the long-term support from the National Natural Science Foundation of China (21222603, U1162107), Ministry of Science and Technology of China

(2013BAC12B01), and Strategic Priority Research Program of Chinese Academy of Sciences (XDA07080301).

Notation

B = baffle width, m
 C = impeller off-bottom clearance, m
 D = impeller diameter, m
 D_C = cavern diameter, m
 F = total force imparted by impeller, N
 F_a = axial force imparted by impeller, N
 H = height of fluid in vessel, m
 H_C = cavern height, m
 k = fluid consistency coefficient, Pa s^n
 K = ratio of wall friction force to yield stress, dimensionless
 k_s = constant used in the Metzner–Otto relationship, dimensionless
 n = flow behavior index, dimensionless
 N = rotational speed, s^{-1}
 N_f = axial force number, dimensionless
 N_p = power number, dimensionless
 N_Q = flow number, dimensionless
 P = power input, W
 Q = impeller pumping rate, $\text{m}^3 \text{s}^{-1}$
 r_C = cavern radius, m
 Re = Reynolds number, dimensionless
 S = impeller spacing, m
 S_p = surface of cavern-stagnant regime, m^2
 S_v = surface of cavern-vessel, m^2
 T = tank diameter, m

Greek letters

α = ellipse parameter in the elliptical torus model, dimensionless
 β = ratio of the major axis to the minor axis of an ellipse in the elliptical torus model, dimensionless
 $\dot{\gamma}$ = shear rate, s^{-1}
 μ = viscosity, Pa s^{-1}
 ρ = fluid density, kg m^{-3}
 τ = shear stress, Pa
 τ_y = yield stress, Pa
 τ_w = wall friction force per unit area, Pa

Abbreviations

CFD = computational fluid dynamics
CMC = carboxymethyl cellulose
ERT = electrical resistance tomography
LDA = laser Doppler anemometry
MRF = multiple reference frame
PBT = pitched blade turbine
PEPI = positron emission projection imaging

PIV = particle image velocimetry
 PLIF = planar laser-induced fluorescence
 RANS = Reynolds-averaged Navier–Stokes
 UDV = ultrasonic Doppler velocimetry

Literature Cited

- Joshi JB, Nere NK, Rane CV, Murthy BN, Mathpati CS, Patwardhan AW, Ranade VV. CFD simulation of stirred tanks: comparison of turbulence models. Part I: radial flow impellers. *Can J Chem Eng*. 2011;89(1):23–82.
- Nere NK, Patwardhan AW, Joshi JB. Liquid-phase mixing in stirred vessels: turbulent flow regime. *Ind Eng Chem Res*. 2003;42(12):2661–2698.
- Bakker CW, Meyer CJ, Deglon DA. Numerical modelling of non-Newtonian slurry in a mechanical flotation cell. *Miner Eng*. 2009;22(11):944–950.
- Gabelle JC, Morchain J, Anne-Archard D, Augier F, Liné A. Experimental determination of the shear rate in a stirred tank with a non-newtonian fluid: carbopol. *AIChE J*. 2013;59(6):2251–2266.
- Adams LW, Barigou M. CFD analysis of caverns and pseudo-caverns developed during mixing of non-newtonian fluids. *Chem Eng Res Des*. 2007;85(5):598–604.
- Arratia P, Kukura J, Lacombe J, Muzzio F. Mixing of shear-thinning fluids with yield stress in stirred tanks. *AIChE J*. 2006;52(7):2310–2322.
- Patel D, Ein-Mozaffari F, Mehrvar M. Dynamic performance of continuous-flow mixing of pseudoplastic fluids exhibiting yield stress in stirred reactors. *Ind Eng Chem Res*. 2011;50(15):9377–9389.
- Solomon J, Elson T, Nienow A, Pace G. Cavern sizes in agitated fluids with a yield stress. *Chem Eng Commun*. 1981;11(1–3):143–164.
- Mavros P. Flow visualization in stirred vessels: a review of experimental techniques. *Chem Eng Res Des*. 2001;79(2):113–127.
- Elson T, Cheesman D, Nienow A. X-ray studies of cavern sizes and mixing performance with fluids possessing a yield stress. *Chem Eng Sci*. 1986;41(10):2555–2562.
- Galindo E, Nienow AW. Performance of the Scaba 6SRGT agitator in mixing of simulated xanthan gum broths. *Chem Eng Technol*. 1993;16(2):102–108.
- Amanullah A, Hjorth SA, Nienow AW. Cavern sizes generated in highly shear thinning viscous fluids by SCABA 3SHP1 impellers. *Food Bioprod Process*. 1997;75(4):232–238.
- Amanullah A, Hjorth SA, Nienow AW. A new mathematical model to predict cavern diameters in highly shear thinning, power law liquids using axial flow impellers. *Chem Eng Sci*. 1998;53(3):455–469.
- Galindo E, Nienow AW. Mixing of highly viscous simulated xanthan fermentation broths with the lightnin A-315 impeller. *Biotechnol Prog*. 1992;8(3):233–239.
- Jaworski Z, Pacek A, Nienow A. On flow close to cavern boundaries in yield stress fluids. *Chem Eng Sci*. 1994;49(19):3321–3324.
- Hirata Y, Aoshima Y. Formation and growth of cavern in yield stress fluids agitated under baffled and non-baffled conditions. *Chem Eng Res Des*. 1996;74(4):438–444.
- Hirata Y, Nienow AW, Moore IPT. Estimation of cavern sizes in a shear-thinning plastic fluid agitated by a Rushton turbine based on LDA measurements. *J Chem Eng Jpn*. 1994;27(2):235–237.
- Saeed S, Ein-Mozaffari F, Upreti SR. Using computational fluid dynamics modeling and ultrasonic doppler velocimetry to study pulp suspension mixing. *Ind Eng Chem Res*. 2007;46(7):2172–2179.
- Ein-Mozaffari F, Upreti SR. Using ultrasonic doppler velocimetry and CFD modeling to investigate the mixing of non-Newtonian fluids possessing yield stress. *Chem Eng Res Des*. 2009;87(4):515–523.
- Pakzad L, Ein-Mozaffari F, Chan P. Using electrical resistance tomography and computational fluid dynamics modeling to study the formation of cavern in the mixing of pseudoplastic fluids possessing yield stress. *Chem Eng Sci*. 2008;63(9):2508–2522.
- Simmons M, Edwards I, Hall J, Fan X, Parker D, Stitt E. Techniques for visualization of cavern boundaries in opaque industrial mixing systems. *AIChE J*. 2009;55(11):2765–2772.
- Hui LK, Bennington CPJ, Dumont GA. Cavern formation in pulp suspensions using side-entering axial-flow impellers. *Chem Eng Sci*. 2009;64(3):509–519.
- Elson T. The growth of caverns formed around rotating impellers during the mixing of a yield stress fluid. *Chem Eng Commun*. 1990;96:303–319.
- Nienow A, Elson T. Aspects of mixing in rheologically complex fluids. *Chem Eng Res Des*. 1988;66(1):5–15.
- Wilkins R, Miller J, Plummer J, Dietz D, Myers K. New techniques for measuring and modeling cavern dimensions in a Bingham plastic fluid. *Chem Eng Sci*. 2005;60(19):5269–5275.
- Rivera C, Foucault S, Heniche M, Espinosa-Solares T, Tanguy PA. Mixing analysis in a coaxial mixer. *Chemical Engineering Science*. 2006;61(9):2895–2907.
- Chew CM, Ristic RI, Reynolds GK, Ooi RC. Characterisation of impeller driven and oscillatory mixing by spatial and temporal shear rate distributions. *Chem Eng Sci*. 2004;59(7):1557–1568.
- Nouri JM, Hockey R. Flow characteristics of Newtonian and non-Newtonian fluids in a vessel stirred by a 60 pitched blade impeller. *Int J Multiphys*. 2008;2(1):83–105.
- Anne-Archard D, Marouche M, Boisson HC. Hydrodynamics and Metzner–Otto correlation in stirred vessels for yield stress fluids. *Chem Eng J*. 2006;125(1):15–24.
- Metzner A, Otto R. Agitation of non-Newtonian fluids. *AIChE J*. 1957;3(1):3–10.
- Nienow A. On impeller circulation and mixing effectiveness in the turbulent flow regime. *Chem Eng Sci*. 1997;52(15):2557–2565.
- Fluent. Fluent 6.3 User's Guide. Lebanon, NH: Fluent Inc., 2006.

Manuscript received Dec. 25, 2013, and revision received Mar. 9, 2014.